Brazilian Journal of Geophysics (2022) 40(Suppl. 1): 1–13

ISSN 2764-8044
DOI 10.22564/brjg.v40i5.2143

AMPLITUDE BEHAVIOR IN LOW-RANK ACOUSTIC MODELING

Jörg Schleicher [1,3*], Jessé Carvalho Costa [2,3], Amélia Novais [1,3], and Andres Valentino Landeta B. [1,3]

[1]Universidade Estadual de Campinas - Unicamp, DMA/IMECC, Campinas, SP, Brazil
[2]Universidade Federal do Pará - UFPA, FAGEOF, Belém, PA, Brazil
[3]National Institute of Science and Technology of Petroleum Geophysics - INCT-GP/CNPq

[*]Corresponding author: js@ime.unicamp.br

ABSTRACT. The numerical simulation of wave propagation can be represented by a propagator matrix applied to previous instances of the wavefield. Using the sparsity of the propagator matrix to approximate it by a low-rank representation, one can increment the wavefield's phase from one time instance to another. Though this procedure does not pay attention to the amplitudes of the seismic waves, it is important to understand its dynamic properties. Here, we evaluate the amplitudes obtained by the low-rank method in the simulation of 2D acoustic wave propagation. In homogeneous media, where theoretical expressions for the wavefield are available, the method provides not only an excellent kinematic approximation, but also reliable amplitudes. For a single horizontal reflector below a homogeneous overburden, the reflection coefficients approximated by the low-rank method are of the same quality or slightly superior to those obtained by a second-order finite-difference (FD) method (implementation from Seismic Un*x). However, in more generally inhomogeneous media, our tests showed larger discrepancies between FD and low-rank modeling results. While comparing unfavorably with FD regarding computation time for small models, its quasi-linear scaling with model size makes the low-rank method superior for large models. Moreover, a generalization to more complex media, e.g., anisotropic, is straightforward.

Keywords: exploration geophysics, mathematical modeling, numerical modeling, wave numerical modeling, computational simulation

INTRODUCTION

Seismic modeling is an important task not only in forward seismic problems, but also in imaging and inversion. Since the analytical solution of the wave equation is only possible in very simple media, numerical approximations are needed to approximate the wavefields in realistic media. The most used methods include approximations by finite differences (FD) (see, e.g., Etgen, 1986) or spectral methods (see, e.g., Palacz, 2018). Both types of methods are well-established and are known to provide reliable estimates of the wavefields under consideration.

A relatively recent method is the modeling of wave propagation by the low-rank method. It describes wave propagation by means of an evolution operator in the mixed space-wavenumber domain that takes the wavefield from one instance of time to the next one. The discretized version of the evolution operator is the so-called propagator matrix. This is a very large matrix of the size "dimension of the space domain" times "dimension of the wavenumber domain". To make its application numerically feasible, the low-rank decomposition makes use of the sparsity of the propagator matrix, selecting a lower-dimensional set of representative spatial locations and a lower-dimensional set of representative wavenumbers (Fomel et al., 2013).

Because of its conceptual simplicity and appeal, the low-rank method has already found a sizeable number of applications. Examples include irregular seismic data reconstruction (Ma, 2013), wavefield extrapolation (Wu and Alkhalifah, 2014), elastic wave-mode separation (Cheng and Fomel, 2014; Wang

et al., 2018), viscoacoustic modeling and imaging (Sun et al., 2015), denoising (Siahsar et al., 2016; Liu et al., 2019), diffraction imaging (Zhao et al., 2020), potential field data separation (Zhu et al., 2020), representation of extended image volumes (Yang et al., 2021), and qP Born scattering simulation (Araújo et al., 2021).

In this work, we evaluate the performance of the low-rank method for numerically approximating the wave propagation in 2D acoustic media. Although the method is derived based on kinematic arguments, we are particularly interested in evaluating its dynamic behavior.

THE PHASE-SHRINKAGE FILTERING METHOD

The acoustic wave equation with constant density is given by

$$\frac{\partial^2}{\partial t^2}P(\mathbf{x},t) = v^2\nabla^2 P(\mathbf{x},t), \tag{1}$$

where $v = v(\mathbf{x})$ denotes the (generally spatially variable) propagation velocity; P the acoustic wavefield; and ∇^2 is the Laplacian. If the velocity is constant, one can solve the wave equation by applying the spatial Fourier transform, defined in this paper as

$$\hat{P}(\mathbf{k},t) = \frac{1}{(2\pi)^3}\int_{-\infty}^{\infty} P(\mathbf{x},t)e^{-i\,\mathbf{x}\cdot\mathbf{k}}d\mathbf{x}. \tag{2}$$

Considering the outward propagating solution to the resulting ordinary differential equation in time, given a fixed initial t_0, the acoustic pressure at $t = t_0 + \Delta t$ for any arbitrary Δt can be exactly represented by means of the inverse Fourier transform as (Etgen and Brandsberg-Dahl, 2009)

$$P(\mathbf{x},t_0+\Delta t) = \int_{-\infty}^{\infty}\hat{P}(\mathbf{k},t_0)e^{i\,[\mathbf{x}\cdot\mathbf{k}+vk\Delta t]}d\mathbf{k}. \tag{3}$$

where $k = \|\mathbf{k}\|$.

If the velocity is not constant, equation 3 is no longer exact. However, it can be generalized using the candidate (Wards et al., 2008)

$$P(\mathbf{x},t_0+\Delta t) = \int_{-\infty}^{\infty}\hat{P}(\mathbf{k},t_0)e^{i\phi(\mathbf{x},\mathbf{k},\Delta t)}d\mathbf{k}, \tag{4}$$

where $\phi(\mathbf{x},\mathbf{k},\Delta t)$ represents a generalized phase function defined in the mixed space-wavenumber domain. It is evident from equation 4 that this is a candidate which tries to superimpose wavefields so that their kinematics are correctly represented. Therefore, it may be possible that it does not correctly describe the dynamics of wave propagation.

Substituting the second temporal and spatial derivatives of the candidate 4 for a fixed t_0 and variable Δt into the wave equation 1, one obtains

$$\left(i\frac{\partial^2\phi}{\partial t^2} - \left(\frac{\partial\phi}{\partial t}\right)^2\right)\hat{P}(\mathbf{k},t_0)e^{i\phi(\mathbf{x},\mathbf{k},\Delta t)} = v^2\left(i\nabla^2\phi - |\nabla\phi|^2\right)\hat{P}(\mathbf{k},t_0)e^{i\phi(\mathbf{x},\mathbf{k},\Delta t)} \tag{5}$$

which is honored if ϕ satisfies the following two differential equations:

$$\left(\frac{\partial\phi}{\partial t}\right)^2 = v^2|\nabla\phi|^2, \tag{6}$$

$$\frac{\partial^2\phi}{\partial t^2} = v^2\nabla^2\phi. \tag{7}$$

Let us start the analysis with the first expression, equation 6. Extracting the square root, we find that ϕ must satisfy

$$\frac{\partial\phi}{\partial t} = \pm v|\nabla\phi|, \tag{8}$$

where we choose the positive sign, which is associated with the outward propagation direction.

Since we are interested in an approximation for small time steps Δt, we now consider the Taylor series of the phase function around $\Delta t = 0$

$$\phi(\mathbf{x},\mathbf{k},\Delta t) = \phi_0(\mathbf{x},\mathbf{k}) + \phi_1(\mathbf{x},\mathbf{k})\Delta t + \phi_2(\mathbf{x},\mathbf{k})\frac{\Delta t^2}{2} + O(\Delta t^3), \tag{9}$$

where

$$\phi_n(\mathbf{x},\mathbf{k}) = \left.\frac{\partial^n\phi}{\partial t^n}\right|_{\Delta t=0}. \tag{10}$$

The zero-order term of the phase function is obtained from substituting $\Delta t = 0$ in equation 4. In this case, the equation must reduce to the inverse Fourier transform, which implies that

$$\phi_0(\mathbf{x},\mathbf{k}) = \phi(\mathbf{x},\mathbf{k},0) = \mathbf{x}\cdot\mathbf{k}. \tag{11}$$

It follows that ϕ can be written as

$$\phi(\mathbf{x},\mathbf{k},\Delta t) = \mathbf{x}\cdot\mathbf{k} + \phi_1(\mathbf{x},\mathbf{k})\Delta t + \phi_2(\mathbf{x},\mathbf{k})\frac{\Delta t^2}{2} + O(\Delta t^3). \tag{12}$$

The terms ϕ_1 and ϕ_2 can be determined from using equation 8. By calculating the gradient with respect to $\mathbf{x}$ of expression 12, multiplying it with itself and taking the square root, it is possible to obtain a linear approximation for its norm, given by

$$|\nabla\phi| \approx k + \frac{\nabla\phi_1\cdot\mathbf{k}}{k}\Delta t. \tag{13}$$

On the other hand, the time derivative of the Taylor series 12 up to first order is

$$\frac{\partial\phi}{\partial t} \approx \phi_1(\mathbf{x},\mathbf{k}) + \phi_2(\mathbf{x},\mathbf{k})\Delta t. \tag{14}$$

Substituting approximations (13) and (14) in (8) and equating the terms of equal powers of Δt results in

$$\phi_1(\mathbf{x},\mathbf{k}) = vk, \tag{15}$$

and

$$\phi_2(\mathbf{x},\mathbf{k}) = v\frac{\nabla\phi_1\cdot\mathbf{k}}{k} = v\frac{\nabla(vk)\cdot\mathbf{k}}{k} = v\,\nabla v\cdot\mathbf{k}. \tag{16}$$

Using these last two expressions in equation 12, we find, up to second order in Δt, that

$$\phi(\mathbf{x},\mathbf{k},\Delta t) \approx \mathbf{x}\cdot\mathbf{k} + v(\mathbf{x})k\Delta t + v(\mathbf{x})\,\nabla v\cdot\mathbf{k}\,\frac{\Delta t^2}{2}. \tag{17}$$

This expression demonstrates that for sufficiently small time steps Δt, particularly in media with smooth velocity variations, the phase function can be approximated up to first order as

$$\phi(\mathbf{x},\mathbf{k},\Delta t) \approx \mathbf{x}\cdot\mathbf{k} + v(\mathbf{x})k\Delta t\ , \tag{18}$$

which results in the final expression

$$P(\mathbf{x},t_0+\Delta t) \approx \int_{-\infty}^{\infty}\hat{P}(\mathbf{k},t_0)e^{i[\mathbf{x}\cdot\mathbf{k}+v(\mathbf{x})k\Delta t]}d\mathbf{k} \tag{19}$$

for the propagator operation. We recognize that this is the same form as the one of equation 3, previously derived by Etgen and Brandsberg-Dahl (2009) for a homogeneous medium. From the above derivation of Fomel et al. (2013), we recognize that it remains approximately valid for inhomogeneous media with smooth velocity variations and/or for small time steps. The neglected second-order term indicates under which assumptions the approximation is valid.

Note that equation 7 was not used in the above derivation. It provides a second validity condition for the linear approximation 18. Because in this approximation the second time derivative of ϕ vanishes, so must its Laplacian, which corresponds to the Laplacian of the velocity field multiplied with the time step.

It is to be stressed that the form of the phase function in equation (18) is particularly attractive because it immediately allows generalizing the approximation (4). It remains applicable when one has a closed expression for the phase velocity in the mixed space $(\mathbf{x},\mathbf{k})$, i.e., $v = v(\mathbf{x},\mathbf{k})$, as it is the case in several classes of anisotropic media. Then, equation 19 becomes

$$P(\mathbf{x},t_0+\Delta t) \approx \int_{-\infty}^{\infty}\hat{P}(\mathbf{k},t_0)e^{i[\mathbf{x}\cdot\mathbf{k}+v(\mathbf{x},\mathbf{k})k\Delta t]}d\mathbf{k}. \tag{20}$$

In this paper, we study a numerical implementation of the low-rank approximation of the acoustic form in equation 19 for 2D constant-density media. Further studies will be necessary to check whether the findings reported here are valid for the more general form of equation 20. However, it is immediately clear that a theoretical generalization is required for variable-density media, because equation 20 does not include any density information.

While equation (19) could be directly applied for wave propagation, it can be modified to avoid a complex propagator matrix. Fomel et al. (2013) suggest adding the corresponding expression for the wavefield at $t_0-\Delta t$, i.e., $P(\mathbf{x},t_0-\Delta t)$ to equation 19 to express the propagator term as a cosine function. In our implementation, we use a slightly different form, subtracting also $2P(\mathbf{x},t_0)$. In this way, the wavefield at $t_0+\Delta t$ can be expressed as

$$\begin{aligned}P(\mathbf{x},t_0+\Delta t) \approx\ & 2P(\mathbf{x},t_0) - P(\mathbf{x},t_0-\Delta t)\\ & + 2\int\hat{P}(\mathbf{k},t_0)e^{i\mathbf{x}\cdot\mathbf{k}}[\cos\left(v(\mathbf{x})\|\mathbf{k}\|\Delta t\right)-1]d\mathbf{k}.\end{aligned} \tag{21}$$

In addition to relying on a real-valued propagator matrix, this form helps to stabilize the numerical computations.

As we can see from equation (4), the basic idea of this wave-propagation procedure is based on kinematic considerations, superimposing wavefields in a kinematically correct way in order to predict the wavefield at a later time. However, being an approximate generalization of equation (3), which is an exact solution of the acoustic wave equation for constant v, we can expect an approximately correct dynamic behavior. It is for this reason that we performed our numerical experiments to evaluate the dynamics of this approximation.

Wave extrapolation matrix

By discretizing the equation (21), we can write it as

$$P_{j,s+1} = 2P_{j,s} - P_{j,s-1} + \sum_l \Delta\mathbf{k}W_{jl}\hat{P}_{l,s}e^{i\mathbf{x}_j\cdot\mathbf{k}_l} \tag{22}$$

where $P_{j,s} = P(\mathbf{x}_j,t_s)$; $\hat{P}_{l,s} = P(\mathbf{k}_l,t_s)$; and W_{jl} denotes the wave extrapolation matrix, defined by

$$W_{jl} = W(\mathbf{x}_j,\mathbf{k}_l) \approx 2[\cos\left(v(\mathbf{x}_j,\mathbf{k}_l)\|\mathbf{k}_l\|\Delta t\right)-1]. \tag{23}$$

Matrix $\mathbf{W}$ has dimension $N_x\times N_k$, where N_x and N_k are the dimensions of the vectors $\mathbf{x}$ and $\mathbf{k}$, respectively, i.e., the dimensions of the full model and wavenumber spaces (in 2D, $N_x = n_x\times n_z$ and $N_k = n_{k_x}\times n_{k_z}$), because $\mathbf{W}$ depends on the spatial and spectral variables. Thus, $\mathbf{W}$ is a rather large matrix. Fortunately, it is very sparse.

The goal of the low-rank method is to take advantage of this sparsity and decompose the matrix using smaller-dimension matrices. That is, an approximate factorization of (23) is sought, with fixed Δt, of the form

$$W(\mathbf{x}_j,\mathbf{k}_l) \approx \sum_{m=1}^{M_k}\sum_{n=1}^{M_x}U(\mathbf{x}_j,\mathbf{k}_m)M_{mn}V(\mathbf{x}_n,\mathbf{k}_j), \tag{24}$$

where M_x and M_k are significantly smaller dimensions than N_x and N_k. Substituting (24) into (22), we obtain

$$P_{j,s+1} = 2P_{j,s} - P_{j,s-1} + \sum_{m=1}^{M_k} U_{jm} \left[\sum_{n=1}^{M_x} M_{mn} \sum_{l} \Delta \mathbf{k} V_{nl} \hat{P}_{l,s} e^{i \mathbf{x}_j \cdot \mathbf{k}_l} \right], \quad (25)$$

where the innermost sum is the discrete Fourier transform of $V_{n,l}\hat{P}_{l,s}$. Because of the significantly lower dimensions of the inner matrix M_{mn}, the number of floating point operations in equation (25) is greatly reduced.

Note that the method is particularly interesting if several shots are to be modeled in the same medium, because the decomposition 24 depends only on the velocity distribution in the model, but not on the wavefield. Therefore, the same propagator matrix is applied to any wavefield propagating in the same model, meaning that the matrix decomposition 24 needs to be performed only once for all wavefields to be propagated.

Low-rank decomposition

Here, we describe the procedure to find an adequate representation of the inner matrix M_{mn} and the transformation matrices U_{jm} and V_{nl}. It follows the description of Fomel et al. (2013) and is based on the method of Engquist and Ying (2007, 2009).

The idea of the low-rank method is to find a low-rank approximation of a sparse matrix $\mathbf{W}$ of rank r, defined by the factorization 24 or, in matrix notation,

$$\mathbf{W} \approx \mathbf{U}\mathbf{M}\mathbf{V}^*, \quad (26)$$

where $*$ denotes the adjoint matrix, i.e., the conjugate of the transposed matrix. Here, $\mathbf{U}$ is a rectangular matrix in the wavenumber domain with N_k rows but only $M_k \ll N_k$ columns. Correspondingly $\mathbf{V}^*$ is a rectangular matrix in the spatial domain with N_x columns but only $M_x \ll N_x$ columns. Since $\mathbf{W}$ is supposed to have a small rank r, we can take $M_k = M_x = r$. Then, $\mathbf{M}$ is a $r \times r$ matrix with complete rank equal to r.

The submatrices $\mathbf{U}$ and $\mathbf{V}^*$, both orthonormal, are constructed such that the columns of $\mathbf{U}$ and the rows of $\mathbf{V}^*$ can accurately generate the column space and the row space of $\mathbf{W}$, respectively. The algorithm to find these matrices starts by randomly selecting a subset $\Omega_1 \subset \{\mathbf{k}\}$ of points in the wavenumber domain, defining a sufficiently large number of columns of $\mathbf{W}$. According to Fomel et al. (2013), 3 or 4 times the expected rank r of $\mathbf{W}$ should be sufficient. In all our numerical tests with homogeneous and inhomogeneous models, it was always enough to use 100 columns. We denote the resulting restricted rectangular matrix by $\mathbf{W}(\{\mathbf{x}\}, \Omega_1)$, so as to indicate that it has the full dimension N_x of the complete set $\{\mathbf{x}\}$ of points in the spatial domain, but only a smaller number of randomly selected columns.

To obtain the largest possible r-dimensional parallelepiped described by $\mathbf{W}(\{\mathbf{x}\}, \Omega_1)$, we compute its QR decomposition with column pivoting (Meyer, 2000). In our numerical experiments, the resulting rank r was estimated by the following stopping criterion: If the ratio between the first and the current pivot of the QR factorization is smaller than a condition number (we used 10^{-6}), the decomposition is stopped and the rank r is equal to the number of pivots in the previous step. Thus, we have $\mathbf{Q}_1$ from

$$\mathbf{W}(\{\mathbf{x}\}, \Omega_1)\mathbf{P}_1 = \mathbf{Q}_1\mathbf{R}_1, \quad (27)$$

where $\mathbf{P}_1$ is the column permutation matrix; $\mathbf{Q}_1$ is the orthogonal matrix; and $\mathbf{R}_1$ is the upper triangular matrix. Then, the first r pivot columns of $\mathbf{Q}_1$ will form the matrix $\mathbf{U}$. In practice, it is observed that the volume of the parallelepiped generated by the columns in $\mathbf{U}$ is always close to the maximum possible volume. According to Fomel et al. (2013), this is a consequence of the oscillatory nature of the columns in $\mathbf{W}$.

In analogy to the previous step, the next step of the algorithm consists of choosing a similar-sized set Ω_2 of rows of $\mathbf{W}$ and again searching for the r-dimensional parallelepiped with the largest volume. For this, it computes the QR decomposition with column pivoting of $\mathbf{W}(\Omega_2, \{\mathbf{k}\})^*$ to obtain

$$\mathbf{W}(\Omega_2, \{\mathbf{k}\})^*\mathbf{P}_2 = \mathbf{Q}_2\mathbf{R}_2. \quad (28)$$

It follows that the first r pivot rows of the matrix $\mathbf{Q}_2$ will form the matrix $\mathbf{V}^*$. Since the two steps to determine $\mathbf{U}$ and $\mathbf{V}$ are carried out independently, the numerical values of r obtained from the two procedures may slightly differ. Therefore, we allow for two different ranks r_k and r_x for $\mathbf{U}$ and $\mathbf{V}$, respectively. As a consequence, the matrix $\mathbf{M}$ is allowed to be rectangular of size $r_k \times r_x$.

Once the matrices $\mathbf{U}$ and $\mathbf{V}$ are computed, the next step is to obtain the low-rank matrix $\mathbf{M} : r_k \times r_x$ such that $\mathbf{W} \approx \mathbf{U}\mathbf{M}\mathbf{V}^*$. To reduce the cost of determining the matrix $\mathbf{M}$, Fomel et al. (2013) propose to choose a set Y of s random rows and a set Z of s random columns of $\mathbf{W}$ and minimize

$$\min_{\mathbf{M}} \|\mathbf{W}(Y, Z) - \mathbf{U}(\{\mathbf{x}\}, Y)\mathbf{M}\mathbf{V}^*(Z, \{\mathbf{k}\})\|_F, \quad (29)$$

where $\|.\|_F$ denotes the Frobenius norm. The result of the minimization procedure (29) can be explicitly represented as

$$\mathbf{M} = (\mathbf{U}(\{\mathbf{x}\}, Y))^\dagger \cdot \mathbf{W}(Y, Z) \cdot (\mathbf{V}^*(Z, \{\mathbf{k}\}))^\dagger, \quad (30)$$

where $(\cdot)^\dagger$ indicates the pseudo-inverse. In our implementation, we use the same size of the random sets for the QR decompositions in equations 27 and 28 and

in the minimization in equation 29. The minimization is carried out using the Algebraic Reconstruction Technique (ART, see, e.g., Gordon, 1974).

NUMERICAL TESTS

Homogeneous medium

We start our numerical evaluation of acoustic modeling by means of the low-rank method with tests in a homogeneous medium, where the analytical solution of the wave equation can be represented by the convolution between the source function and the Green's function. Note that in this case, the extrapolator representation 3 is exact, which allows for an evaluation of the quality of the low-rank decomposition 25.

Our first model (called model A) is a 2D homogeneous medium with propagation velocity 2000 m/s, a surface extension of 9000 m and a depth of 4500 m, discretized with a spatial sampling interval $\Delta x = \Delta z = 10$ m. In this way, the spatial dimension of the propagator matrix is $N_x = 901 \times 451 = 406351$. Since the wavenumber space is defined up to the Nyquist frequency, we thus have here $N_k = 451 \times 226 = 101926$.

For the first numerical experiment, we used an injector source located at coordinates $x = 4500$ m, $z = 1000$ m. The maximum propagation time was 2 s with a time sampling interval $\Delta t = 0.001$ s. The receiver is located at the same horizontal coordinate as the source at a depth of 3000 m. The pulse injected into the impulsive source is a causal Ricker wavelet with a peak frequency of 5 Hz. To obtain the reference analytical response as a variation of the wavefield as a function of time, we compute the convolution of this Ricker wavelet with the 2D Green's function,

$$G(x,z,t;x_s,z_s) = \frac{1}{2\pi\sqrt{t^2 - r^2/v^2}} H(t - r/v) \ , \quad (31)$$

where $r = \sqrt{(x-x_s)^2 + (z-z_s)^2}$ and $H(\tau)$ is the Heaviside unit step function.

Figure 1(a) shows the temporal traces of the analytical solution and those obtained using the low-rank method, which show an excellent coincidence. The pulse shape in the two traces is almost identical, with low-rank slightly underestimating the amplitude. The arrival time of the events is indistinguishable and their value of 1 s is correct for the propagation distance of 2000 m in a medium with a velocity of 2000 m/s. The relative dynamic error of the modeling considering the peak of the traces was 0.015 %. The numerically estimated rank r of the propagator matrix was equal to 2.

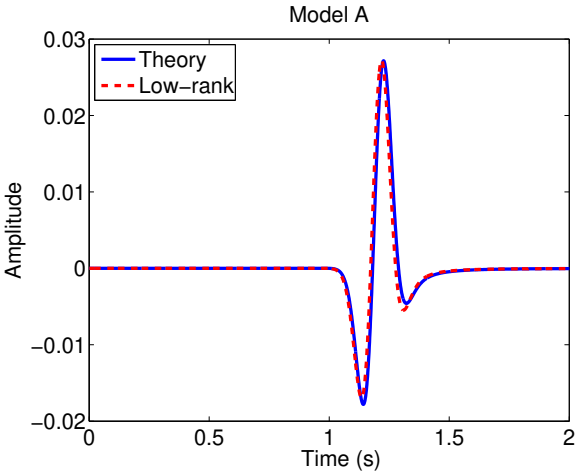

(a)

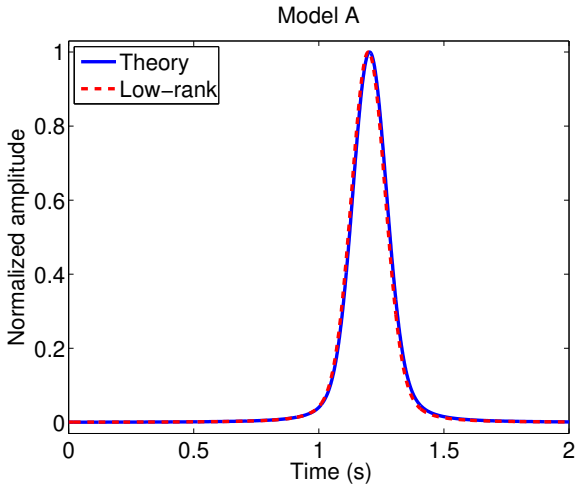

(b)

Figure 1: Comparison of a seismic trace modeled with the low-rank method in model A with $\Delta t = 0.001$ s (dashed red line) to the analytical solution (solid blue line). (a) Traces. (b) Normalized envelopes.

To verify whether the slight differences of the pulses in the traces in Figure 1(a) are the consequence of a kinematic error or a phase error of the modeled pulse, we calculated their normalized envelopes, shown in Figure 1(b). Since the envelopes are virtually identical, we conclude that the traveltime of the pulses is correct, and the fact that the pulses in Figure 1(a) are not fully coincident is due to a small phase difference between the pulses, resulting from numerical errors.

The amplitudes obtained from our implementation of the low-rank decomposition actually were wrong by a frequency-dependent scale factor, which could be easily corrected.

The high quality of the low-rank results is valid over a large range of time sampling intervals and peak frequencies of the source wavelet. Figure 2 shows the values of the peak amplitudes of the modeled trace as a function of time sampling interval (Figure 2a) and peak frequency (Figure 2b).

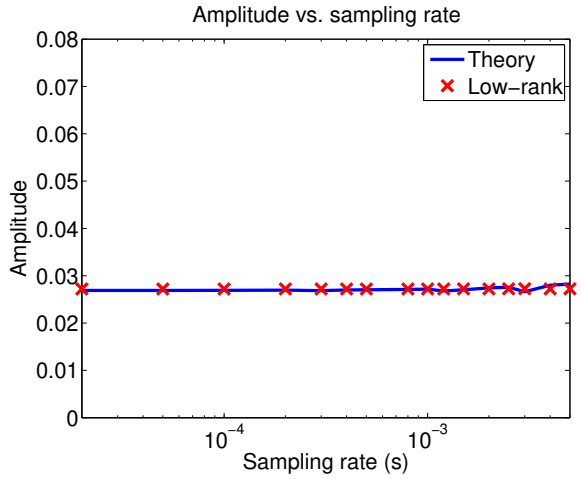

(a)

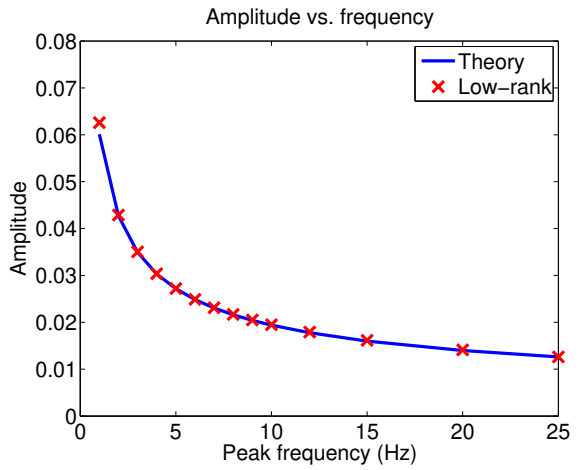

(b)

Figure 2: Peak amplitude of the modeled traces (a) as a function of time sampling interval (for a fixed peak frequency of $f_p = 5$ Hz) and (b) as a function of peak frequency (for a fixed sampling interval of $\Delta t = 0.001$ s).

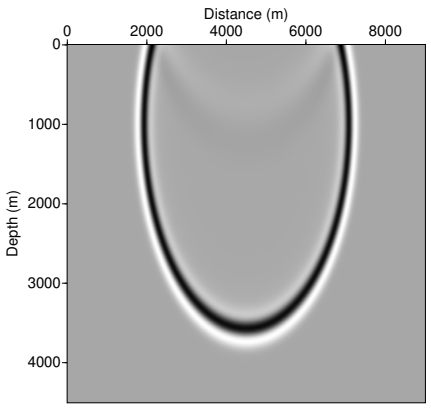

(a)

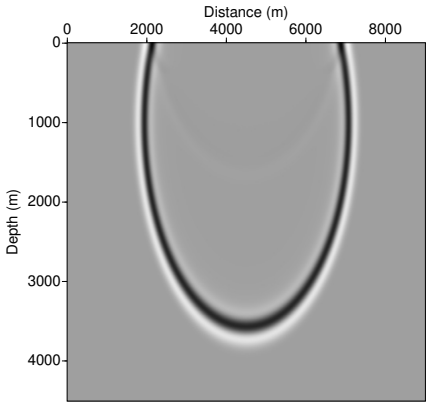

(b)

Figure 3: Wavefield snapshot in model A after 1.5 s for a source located at coordinates $x = 4500$ m, $z = 1000$ m. (a) Low-rank approximation. (b) Finite Differences.

From this experiment, we conclude that the low-rank method is capable of calculating highly accurate numerical approximations to acoustic wave propagation in a homogeneous medium.

Comparison to finite differences

To check whether the quality is comparable with that of the FD method, we compared our results to those obtained with the **sufdmod2** program of Seismic Un*x (SU, see Stockwell and Cohen, 2019). The latter program uses the traditional second-order approximation in time and space for the partial derivatives in the wave equation. Since this program fixes the time sampling interval automatically so that the stability of the method is guaranteed, we used the same Δt for the low-rank method in this comparison.

For this experiment in model A, the SU program fixes the temporal sampling interval at 0.0025 s. Figure 3 shows the snapshot of the propagation at time $t = 1.5$ s, modeled by the low-rank method (Figure3a) and by FD (Figure 3b). We observe two very similar results, highlighting that the only perceptible difference is the different shape of the border reflection at the top, caused by a different quality of the absorbing boundaries.

The amplitude scaling of the modeled wavefield is different, though, as revealed by the comparison of the vertical slices through these snapshots at the horizontal position of the source (compare the low-rank result in Figure 4 to that from FD in Figure 5).

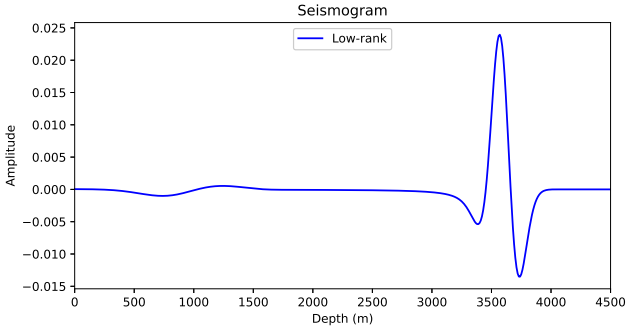

Figure 4: Vertical spatial slice through the low-rank wavefield snapshots at the source position in Figure 3(a).

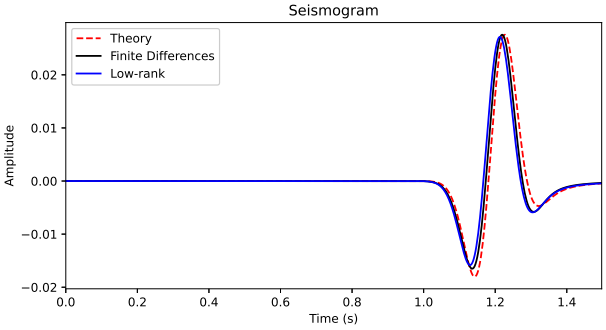

Figure 6: Comparison of the temporal traces of the analytical solution with the solutions obtained using the low-rank and FD methods in model A with $\Delta t = 0.0025$ s.

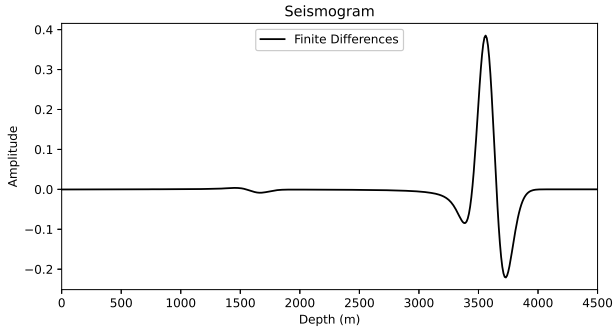

Figure 5: Vertical spatial slice through the FD wavefield snapshots at the source position in Figure 3(b).

We note that the direct wave is kinematically positioned correctly in both slices. The wavelet shapes are very similar, but the amplitudes are different by an order of magnitude. We can also observe the different format and positioning of the boundary reflection. Note that for this example, the FD result is free of any noticeable numerical dispersion. Other spatial discretizations led to perceptible dispersion.

Considering again the receiver located at a distance of 2000 m down from the source, Figure 6 compares the resulting traces of the analytical, low-rank and FD solutions. To be able to plot the traces approximated by the two methods in a single figure, we normalized them by an amplitude scale, determined by the peak amplitude ratio between the analytical solution and the approximate traces. The resulting scale factor for the low-rank method was 1.02 and for FD, 0.06. Note that for the given discretization, the low-rank method slightly underestimates the wave, while the SU FD program considerably overestimates the theoretical solution. Regarding the wavelet shape, we recognize that the solutions of FD and the low-rank approximation are very similar to each other, both presenting a small phase error with respect to the theoretical solution.

Analysis of the Reflection Coefficients

To analyse whether the low-rank method can also well approximate the amplitudes of reflected waves, we devised another experiment with a single planar horizontal reflector (model B). In such a model, the reflection coefficients should be well approximated by the theoretical formulas for the plane wave reflection coefficients.

Our model B has again a horizontal extension of 9000 m and a depth of 4500 m with a spatial sampling of 10 m. It consists of a homogeneous overburden with a wave speed of 2000 m/s and a single planar horizontal reflector at a depth of 2 km. The velocity of the medium below the reflector was 2200 m/s.

To determine the reflection coefficients obtained by the low-rank and FD methods without any perturbation by the direct wave and boundary effects, we performed a sequence of three numerical experiments. The source is located at the same position for all three experiments, being again at $x = 4500$ m, $z = 1000$ m.

For the first experiment we recorded the wave propagating in model B with an arrangement of 200 receivers at the depth of 500 m, spaced 10 m apart with an *end-on spread* configuration, the first receiver being located at zero offset (normal incidence). The second and third experiments consider a homogeneous medium with the same dimensions as model B and a constant wave velocity of the upper part of model B, i.e., 2000 m/s. In the second experiment, we record the wavefield in this homogeneous model at the same receivers of the first experiment, in this way observing the same direct waves (and possible boundary effects). Finally, in the third experiment, we record the wavefield at the mirror receivers, positioned symmetrically to the original receivers with respect to the reflector position. In this way, the propagation distance and thus the traveltime and geometrical spreading to the mirror receivers in the third experiment are the same as for the reflected wave in the first experiment.

Thus, by subtracting the result of the second experiment, which contains only the direct wave and possible boundary reflections, from the result of the first experiment, we extract the reflected event. Dividing this difference by the result of the third experiment, we obtain the approximate reflection coefficients as simulated by the respective method.

In these experiments, we fixed the temporal sampling interval for the low-rank method at 0.001 s, while the one for FD was determined by the program using the stability condition. For model B, the temporal discretization of FD was 0.00227273 s, which was then fixed for all three numerical computations. Figure 7 shows the reflected event recorded at normal incidence after subtracting the direct wave at the true receiver (blue line) and the direct wave at the corresponding mirror receiver (green line) as modeled by the low-rank method. As expected, the events are kinematically coincident. The ratio of these traces defines the modeled reflection coefficient at normal incidence.

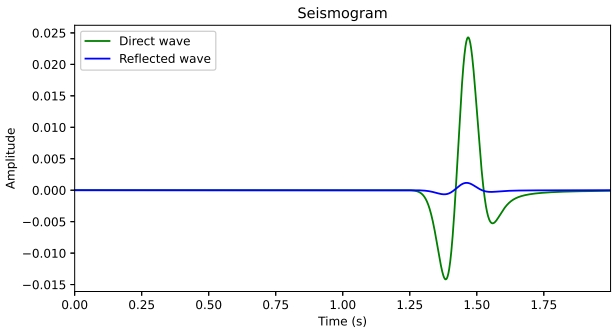

Figure 7: The reflected wave at the true receiver (blue line) and the direct wave at the mirror receiver (green line) share the same kinematics and geometrical spreading. Their amplitude ratio is the reflection coefficient as modeled by the used numerical approximation.

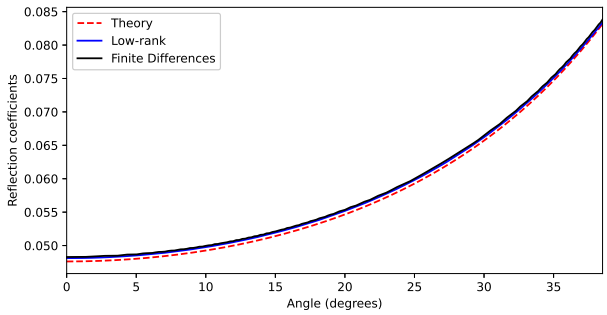

Figure 8: Comparison of theoretical angle-dependent reflection coefficients (dashed red line) with numerical approximations from the low-rank method (solid blue line) and FD (solid black line) for model B ($v_1 = 2000$ m/s and $v_2 = 2200$ m/s).

Correspondingly, the reflection coefficients at other incidence angles are given by the ratios between the reflected wave recorded at the original receivers in model B and the wave recorded at the corresponding mirror receivers in the homogeneous medium. Figure 8 shows the approximations of the reflection coefficients for model B, obtained from low-rank (solid blue line) and FD (solid black line), as compared to the theoretical reflection coefficients (dashed red line).

We notice a very good approximation of the reflection coefficients by the low-rank and FD methods. Actually, comparing the relative errors of the achieved approximations, shown in Figure 9, we can see that the approximation by the low-rank method (blue line) is even somewhat better than the one by FD (black line). Overall, the relative errors of low-rank are lower and show less fluctuation than those of the FD method.

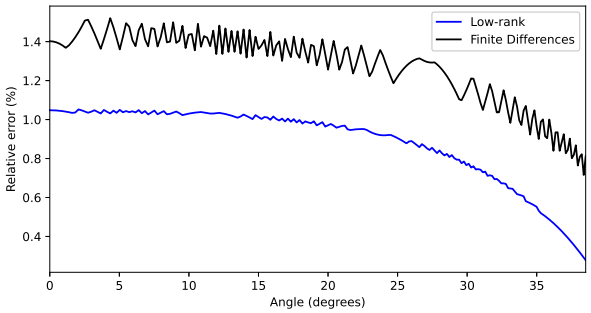

Figure 9: Relative error of the reflection coefficients approximated by the low-rank method (blue line) and FD (black line) for model B ($v_1 = 2000$ m/s and $v_2 = 2200$ m/s).

We have repeated these experiments with the same geometry for other velocity contrasts at the reflector, generally confirming our findings reported here. In almost all cases, the low-rank reflection coefficients are slightly better than the FD ones.

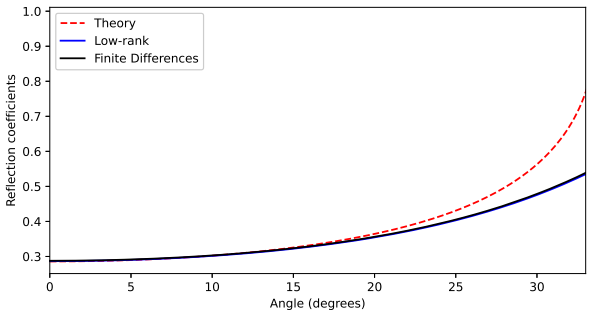

Figure 10: Comparison of theoretical angle-dependent reflection coefficients (dashed red line) with numerical approximations from the low-rank method (solid blue line) and FD (solid black line) for model B' ($v_1 = 2500$ m/s and $v_2 = 4500$ m/s).

Here, we show two typical examples for a larger velocity contrast (model B') with $v_1 = 2500$ m/s and $v_2 = 4500$ m/s (Figures 10 and 11), and a velocity inversion (model B") with $v_1 = 2500$ m/s and $v_2 = 2000$ m/s (Figures 12 and 13). Note that when approaching the critical angle, the modeled reflection coefficients of the FD and low-rank approximations deviate from the theoretical curves in a very similar way (Figure 10). Again, the relative error of the low-rank results is slightly smaller than that from FD (Figure 11).

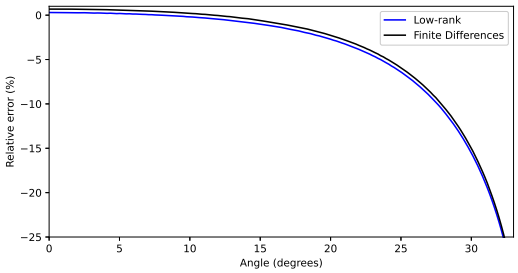

Figure 11: Relative error of the reflection coefficients approximated by the low-rank method (blue line) and FD (black line) for model B' ($v_1 = 2500$ m/s and $v_2 = 4500$ m/s).

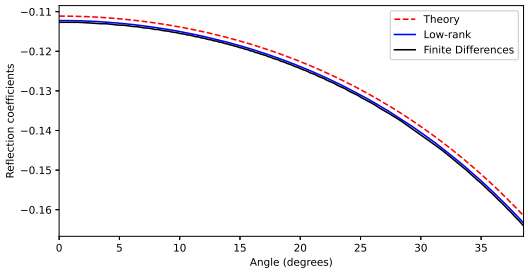

Figure 12: Comparison of theoretical angle-dependent reflection coefficients (dashed red line) with numerical approximations from the low-rank method (solid blue line) and FD (solid black line) for model B" ($v_1 = 2500$ m/s and $v_2 = 2000$ m/s).

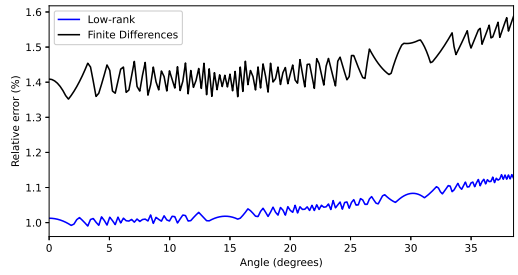

Figure 13: Relative error of the reflection coefficients approximated by the low-rank method (blue line) and FD (black line) for model B" ($v_1 = 2500$ m/s and $v_2 = 2000$ m/s).

We have repeated these experiments for several velocity contrasts at the reflector. Figure 14 shows the relative error of the low-rank reflection coefficients at incidence angles of 0° (solid blue line), 30° (dashed green line) and 45° (dash dotted red line). We see that at normal incidence, the amplitude error is very small for all velocity contrasts. At an incidence angle of 30°, the error is below 10% up to a velocity contrast of 70%. However, the reflection coefficients get wrong close to the critical angle, resulting in rather large errors at 45°.

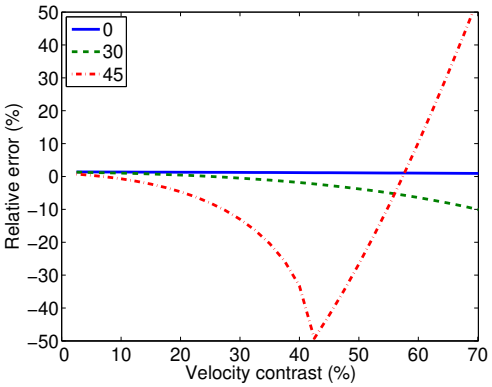

Figure 14: Error of the estimated reflection coefficient as a function of the velocity contrast at the reflector at incidence angles of 0° (solid blue line), 30° (dashed green line) and 45° (dash dotted red line).

Inhomogeneous model

As a more realistic test, we compare the results of low-rank and FD modeling in the Marmousi model (velocity distribution in Figure 15). This model has a grid of 767 × 243 points with a spatial discretization of 12 m. The SU FD modeler fixes the time sampling at $\Delta t = 0.00102604$ s. The low-rank method determines the numerical rank of the propagator matrix again as $r = 2$.

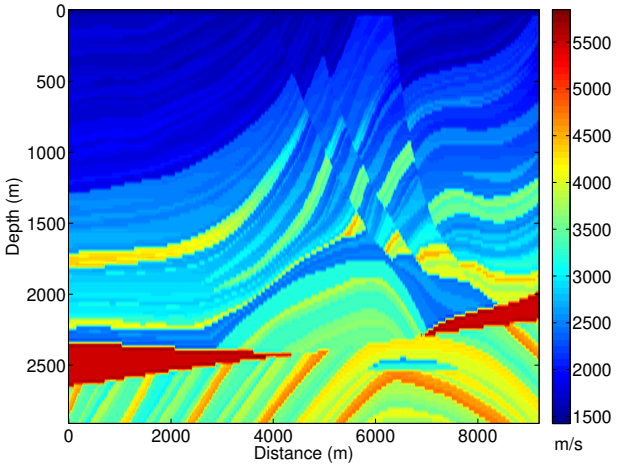

Figure 15: Velocity distribution of the Marmousi model.

Figure 16 compares the snapshots from both methods at 1.5 s for a source at coordinates $x = 4596$ m, $z = 120$ m. Overall, the snapshots are very similar. Relative amplitudes are mostly comparable, apparently indicating that acoustic low-rank modeling is not only kinematically but also dynamically reliable even in more complex media.

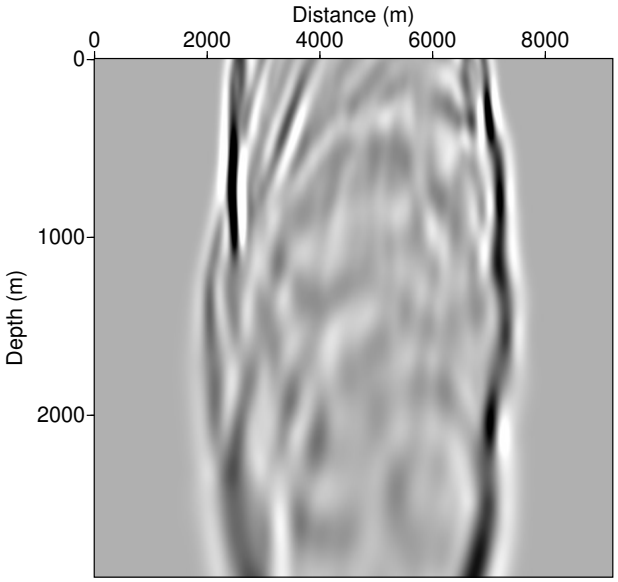

(a)

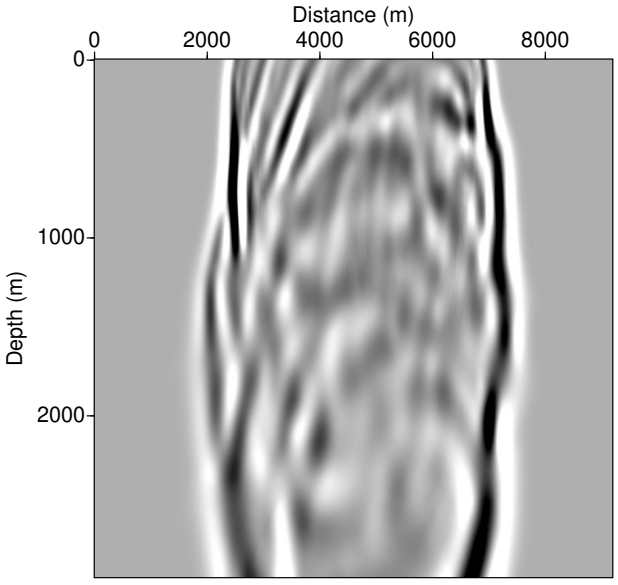

(b)

Figure 16: Snapshot of wave propagation in the Marmousi model at 1.5 s for a source at coordinates $x = 4596$ m, $z = 120$ m. (a) Low-rank approximation. (b) Finite Differences.

Finally, Figure 17 shows the corresponding common-shot sections. Again, overall the sections are rather similar. However, a few differences can be noted at later times. It is unclear whether these must be attributed to cumulative kinematic errors of the low-rank method or to accumulated effects of numerical dispersion and dissipation of the employed FD code. This needs to be investigated in the future using an independent modeling technique.

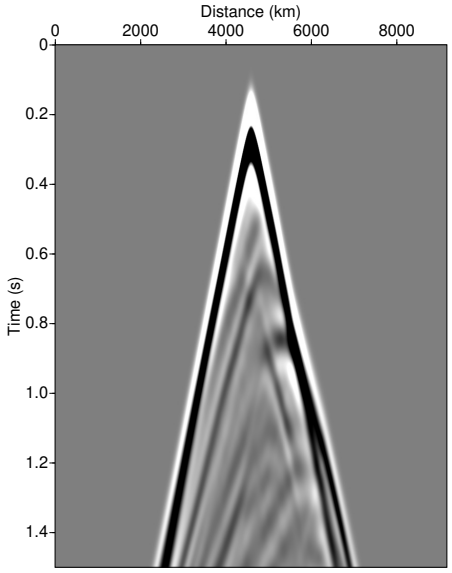

(a)

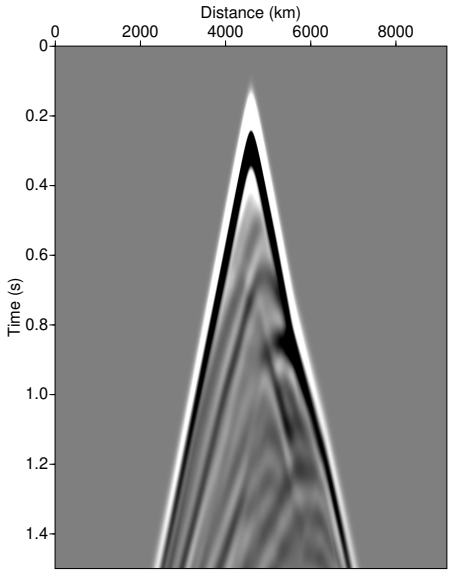

(b)

Figure 17: Common-shot sections in the Marmousi model for a source at coordinates $x = 4596$ m, $z = 120$ m. (a) Low-rank approximation. (b) Finite Differences.

Computation time

To evaluate the computation time of low-rank modeling, we carried out a number of tests in homogeneous media with the same wave velocity of 2000 m/s and physical dimensions, but different spatial sampling and, thus, different grid sizes. Table 1 shows the different models and Figure 18 presents the resulting computation times to model up to two seconds of propagation time.

Table 1: Differently sized models used to evaluate the computation time.

Models	$n_x \times n_z$	$\Delta x = \Delta z$ (m)	Δt (s)
Model 1	181 × 91	50	0.01250
Model 2	451 × 226	20	0.00500
Model 3	601 × 301	15	0.00375
Model 4	901 × 451	10	0.00250
Model 5	1801 × 901	5	0.00125
Model 6	3601 × 1801	2.5	0.00075

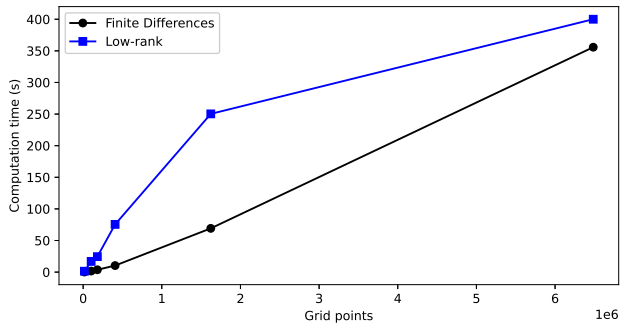

Figure 18: Computation time for low-rank and FD modeling up to two seconds of propagation time in homogeneous models of different grid size (in millions of points).

Although our available computational resources did not allow for the use of larger models, we can already conclude from Figure 18 that low-rank modeling scales more favorably with model size than FD modeling. Thus, for larger models than the ones tested here (or, for that matter, for 3D models), it can be expected that low-rank modeling is computationally less expensive than FD modeling. Note, however, that for inhomogeneous models, the crossing point will be at larger models than for the tests with homogeneous models shown here. For instance, the computation time for our test in the Marmousi model, which used 186381 grid points, was 102 s, clearly exceeding the time in a homogeneous model of the same size.

DISCUSSION AND CONCLUSIONS

By means of numerical experiments in different models, we have evaluated the absolute and relative performance of 2D acoustic modeling using the low-rank method, particularly with regard to the quality of the resulting amplitudes. For the first part of the experiments, we considered homogeneous media, in order to compare the numerical results to the analytical solution of the wave equation. In this way, we studied the response of the low-rank method for various discretizations of the same model and compared it to the theoretical response in kinematics and dynamics. From our tests, we conclude that the kinematic quality of the method is rather good, and that the dynamic results depend on the spatial and temporal discretization, as well as the peak frequency of the employed source wavelet. However, a simple frequency-dependent correction factor allowed producing reliable amplitudes. The reference numerical solution, obtained by the FD code from Seismic Un*x, produced incorrectly scaled amplitudes. Moreover, it is more sensitive to numerical dispersion for coarse spatial discretizations. This also affects the kinematics as the waves tend to arrive slightly earlier than in the theoretical solution. It is to be observed that there is no dispersion effect in low-rank modeling.

In a second set of tests, we evaluated the reflection coefficients modeled by the low-rank method, again in comparison to the SU FD code. Even though the low-rank method does not explicitly include any amplitude effects, the acoustic reflection coefficients are well approximated.

Finally, a test in the Marmousi model also revealed acceptable properties of the modeled wavefields. However, some discrepancies to the FD solutions were visible at larger traveltimes. Further investigation is necessary so as to determine whether these must be attributed to errors of the numerical low-rank or FD solutions.

Summarizing, our tests demonstrated that the low-rank method can produce reliable acoustic wavefields, both regarding traveltimes and amplitudes. This is particularly important for large-scale problems, because the computing cost of low-rank modeling scales much more favorably with model size than that of FD. Future studies will have to be carried out so as to evaluate whether this excellent amplitude behavior can also be achieved in more general media, particularly those exhibiting anisotropy.

ACKNOWLEDGMENTS

The authors are grateful for the support of our working groups by Petrobras as well as the Brazilian agencies CNPq (supporting the INCT-GP) and CAPES (student scholarship).

REFERENCES

Araújo, I., M. Nascimento, J. Costa, A. Souza, and J. Schleicher, 2021, Anisotropic born scattering for the qP scalar wavefield using a low-rank symbol approximation: Geophysics, **86**, T337–T348, doi: 10.1190/geo2020-0764.1.

Cheng, J., and S. Fomel, 2014, Fast algorithms for elastic-wave-mode separation and vector decomposition using low-rank approximation for anisotropic media: Geophysics, **79**, C97–C110, doi: 10.1190/geo2014-0032.1.

Engquist, B., and L. Ying, 2007, Fast directional multilevel algorithms for oscillatory kernels: SIAM Journal on Scientific Computing, **29**, 1710–1737, doi: 10.1137/07068583x.

Engquist, B., and L. Ying, 2009, A fast directional algorithm for high frequency acoustic scattering in two dimensions: Communications in Mathematical Sciences, **7**, 327–345, doi: 10.4310/CMS.2009.v7.n2.a3.

Etgen, J. T., 1986, High-order finite-difference reverse time migration with the 2-way non-reflecting wave equation: SEP Report, **SEP-48**, 133–146.

Etgen, J. T., and S. Brandsberg-Dahl, 2009, The pseudo-analytical method: Application of pseudo-Laplacians to acoustic and acoustic anisotropic wave propagation: SEG Technical Program Expanded Abstracts, **28**, 2552–2556, doi: 10.1190/1.3255375.

Fomel, S., L. Ying, and X. Song, 2013, Seismic wave extrapolation using lowrank symbol approximation: Geophysical Prospecting, **61**, 526–536, doi: 10.1111/j.1365-2478.2012.01064.x.

Gordon, R., 1974, A tutorial on ART (algebraic reconstruction techniques): IEEE Transactions on Nuclear Science, **21**, 78–93, doi: 10.1109/TNS.1974.6499238.

Liu, Z., J. Ma, and X. Yong, 2019, Line survey joint denoising via low-rank minimization: Geophysics, **84**, V21–V32, doi: 10.1190/geo2018-0141.1.

Ma, J., 2013, Three-dimensional irregular seismic data reconstruction via low-rank matrix completion: Geophysics, **78**, V181–V192, doi: 10.1190/geo2012-0465.1.

Meyer, C. D., 2000, Matrix Analysis and Applied Linear Algebra: SIAM. (doi: 10.1137/1.9780898719512).

Palacz, M., 2018, Spectral methods for modelling of wave propagation in structures in terms of damage detection—a review: Applied Sciences, **8**, 1124, doi: 10.3390/app8071124.

Siahsar, M. A. N., S. Gholtashi, A. R. Kahoo, H. Marvi, and A. Ahmadifard, 2016, Sparse time-frequency representation for seismic noise reduction using low-rank and sparse decomposition: Geophysics, **81**, V117–V124, doi: 10.1190/geo2015-0341.1.

Stockwell, Jr., J. W., and J. K. Cohen, 2019, The new SU user's manual. version 4.6: CWP/SU, Center for Wave Phenomena, Colorado School of Mines. USA. (URL: https://nextcloud.seismicunix.org/index.php/s/wZNoFCfJdXj5iKB).

Sun, J., T. Zhu, and S. Fomel, 2015, Viscoacoustic modeling and imaging using low-rank approximation: Geophysics, **80**, A103–A108, doi: 10.1190/geo2015-0083.1.

Wang, W., B. Hua, G. A. McMechan, and B. Duquet, 2018, P- and S-decomposition in anisotropic media with localized low-rank approximations: Geophysics, **83**, C13–C26, doi: 10.1190/geo2017-0138.1.

Wards, B. D., G. F. Margrave, and M. P. Lamoureux, 2008, Phase-shift time-stepping for reverse-time migration: 78th Annual International Meeting, SEG, Expanded Abstracts, 2262–2266. doi: 10.1190/1.3059335.

Wu, Z., and T. Alkhalifah, 2014, The optimized expansion based low-rank method for wavefield extrapolation: Geophysics, **79**, T51–T60, doi: 10.1190/geo2013-0174.1.

Yang, M., M. Graff, R. Kumar, and F. J. Herrmann, 2021, Low-rank representation of omnidirectional subsurface extended image volumes: Geophysics, **86**, S165–S183, doi: 10.1190/geo2020-0152.1.

Zhao, J., C. Yu, S. Peng, and C. Li, 2020, 3D diffraction imaging method using low-rank matrix decomposition: Geophysics, **85**, S1–S10, doi: 10.1190/geo2018-0417.1.

Zhu, D., H. Li, T. Liu, L. Fu, and S. Zhang, 2020, Low-rank matrix decomposition method for potential field data separation: Geophysics, **85**, G1–G16, doi: 10.1190/geo2019-0016.1.

Schleicher, J.: writing, implementation, numerical tests, theoretical revision; **Costa, J.C.:** main implementation, theoretical revision; **Novais, A.:** writing, numerical tests, theoretical revision; **Landeta, B.A.V.:** writing, numerical tests, theoretical revision.

Received on August 1, 2022 / Accepted on November 30, 2022